Journal of Scientific Computing, Vol. 2, No. 3, 1987

Numerical Simulation of Turbulent Spots in Channel and Boundary Layer Flows

Edward T. Bullister[1] and Steven A. Orszag[2]

Received December 17, 1986

The initiation and early growth of spots in channel and boundary layer flows is simulated using a three-dimensional spectral code. The simulated spots show significant agreement with available experimental data for such quantities as growth rates and spreading angles. Disturbances are introduced into the center and edge of the developing channel spots to investigate the relative sensitivity of spots.

KEY WORDS: Turbulent spots; boundary layer; plane Poiseuille flow; transition; channel flow.

1. INTRODUCTION

Emmons (1951) was the first to observe turbulent spots in a laminar flow undergoing transition to a turbulent flow. Since then a large number of investigators have recognized the importance of spots in the study of both transition and turbulence. Naturally occurring spots are initiated by flow disturbances like noise. In the laboratory, spots may be artificially initiated with electric sparks or by injecting a jet of fluid. In a numerical simulation of spots, controlled disturbances may be imposed on a solution of the Navier–Stokes equations.

Soon after Emmons' discovery, Elder (1960) noted that spots tend to grow independently of one another, even when they overlap. Gaster and Grant (1975) studied the linear growth of small amplitude disturbances

[1] Department of Mechanical Engineering, Massachusetts Institute of Technology, Cambridge, Massachusetts 02139.

[2] Applied and Computational Mathematics, Princeton University, Princeton, New Jersey 08544.

0885-7474/87/0900-0263$05.00/0

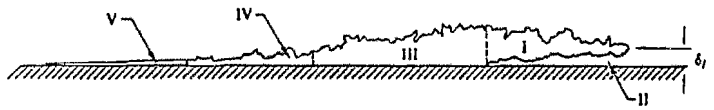

Fig. 1. Schematic of an experimental boundary layer spot cut through the center (from Gad-el-Hak *et al.*, 1981).

into a wave packet using both laboratory experiments and theoretical analysis. Their theoretical predictions have been confirmed by laboratory observations so long as nonlinear effects are not important. Wygnanski, Sokolov, and Friedman (1976) conducted an experimental study of spots in a boundary layer. Using conditional sampling techniques, they mapped out the geometry and growth rates of a spot as it develops in a boundary layer. Gad-el-Hak *et al.* (1981) conducted flow visualization experiments on boundary layer spots by injecting dye upstream of the spot initiation. They divided the spot into five regions (see Fig. 1). Region I within the spot overhangs region II, the laminar boundary layer below the head of the spot. Region III appears similar to a turbulent boundary layer. In

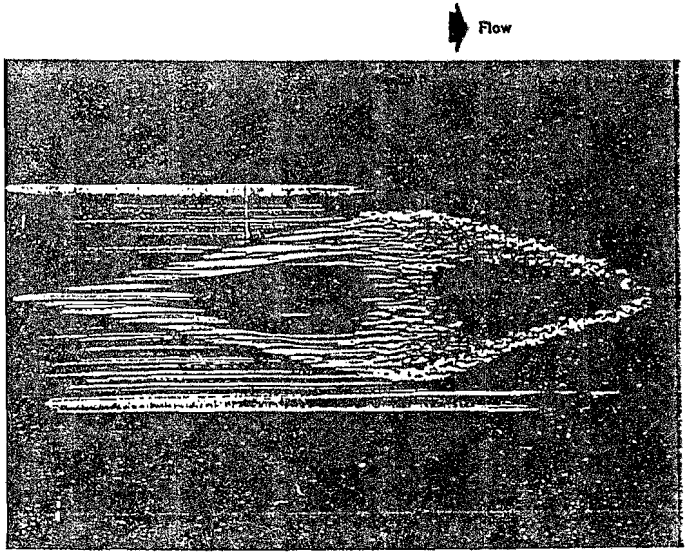

Fig. 2. Visualization of an experimental boundary layer spot using fluorescent dye and a sheet of laser light at the wall; $Re_x = 5 \times 10^5$ (from Gad-el-Hak *et al.*, 1981).

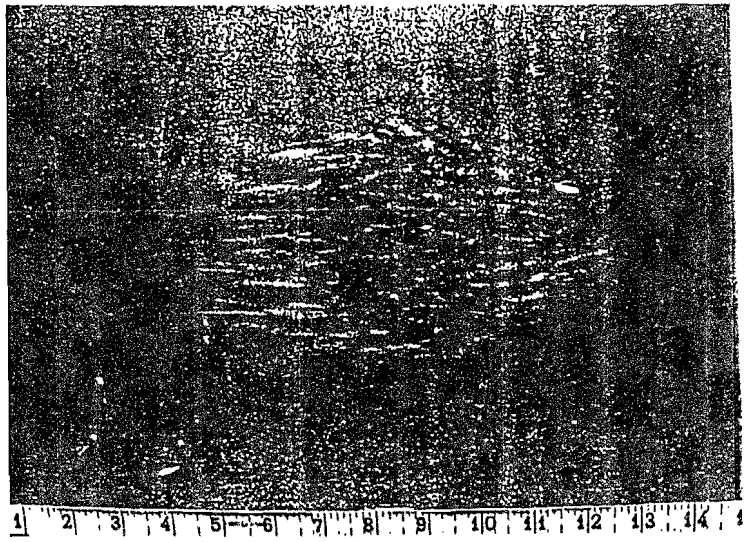

Fig. 3. Visualization of an experimental channel spot using mica platelets (from Carlson *et al.*, 1982).

regions IV and V the flow returns to a "calm" state. The photograph in Fig. 2 illustrates the characteristic arrowhead shape of a boundary layer spot in streamwise–spanwise projection. This photograph was obtained by illuminating dye lines with a sheet of light very close to the wall.

The first detailed research directed toward investigating the characteristics of spots in a channel was conducted by Carlson *et al.* (1982).

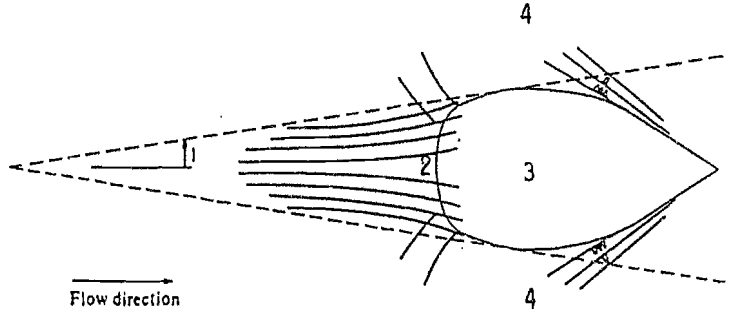

Fig. 4. Channel spot schematic: (1) spreading half-angle; (2) trailing streaks; (3) region of small-scale turbulence; (4) oblique Tollmein-Schlicting waves (from Carlson *et al.*, 1982).

Using mica flakes to visualize the flow (Fig. 3), they observed that a channel spot also has the characteristic arrowhead shape. They identified (see Fig. 4) several features present in channel spots. The spreading half-angle (1) was about 8°. The leading edges met at a sharp point and were preceded by oblique waves (4). The center of the spot (3) contained small-scale turbulence. Streaks (2) trailed behind region 3.

The purpose of the present study is to use direct numerical solution of the Navier–Stokes equations to identify details of the internal structure of spots, as well as to map out spot dimensions and growth rates. Comparison of our results for growth rates of the large-scale spot dimensions with those seen experimentally verifies that the essential growth mechanisms of spots is captured by our numerical experiments.

One previous study of numerical spots should be mentioned. Leonard (1981) used discrete vortex methods to simulate numerically the early growth of a spot in a boundary layer. As with the present computations, the spots computed by Leonard are typically less mature than experimentally observed spots.

2. COMPUTATIONAL GEOMETRIES AND NUMERICAL METHODS

The computational domain that we use to simulate channel flow spots is as follows. In our simulations of channel flow spots, the flow is represented by $128 \times 64 \times 33$ Fourier and Chebyshev modes in the x (streamwise), y (spanwise), and z (normal) directions, respectively (see Fig. 5). The flow satisfies periodic boundary conditions in x and y and no-slip (rigid) boundary conditions at the walls ($z = \pm 1$). The computational box is nondimensionalized by the channel half-width; in the runs presented below, the physical box size is $20 \times 5 \times 2$. With 128×64 resolution in x and y, the resultant node spacing (in physical space) of the spectral collocation points is $\Delta x = 0.16$ and $\Delta y = 0.08$.

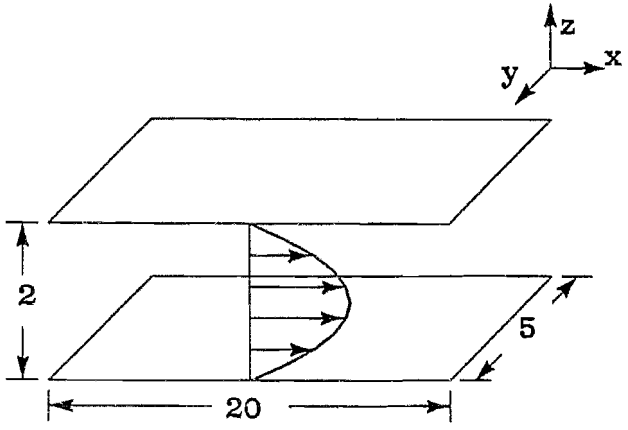

Fig. 5. Channel geometry and nomenclature. Channel is $20 \times 5 \times 2$ in the x, y, and z directions, with 128×64 Fourier modes in x and y and 33 Chebyshev modes in z.

For our boundary layer spot calculations, the flow is represented using 64 Fourier modes in x and y, with $\Delta x = 2$ and $\Delta y = 1$ (see Fig. 6). In the z direction, the 33 collocation points are obtained by an algebraic mapping of the interval $[-1, 1]$ to $[0, \infty]$ with half the collocation points located in the region $0 < z < 5$. The computational box is nondimensionalized by the boundary layer thickness $(\eta = \nu x_0 / U_\infty)^{1/2}$ at some representative x location x_0. The periodic boundary conditions used in the streamwise direction are only approximate. They are justified because the increase in boundary layer thickness through the computational domain is only 6% (see also Balasubramanian *et al.*, 1988). While inflow–outflow boundary conditions are, in principle, more realistic than periodic boundary conditions, they are more wasteful of spatial resolution, which is the limiting factor in the present calculations.

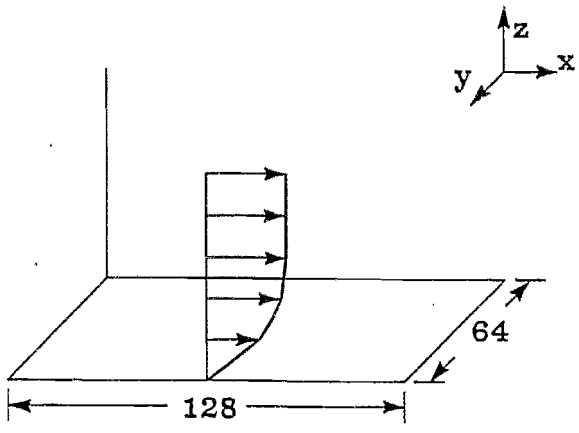

Fig. 6. Boundary layer geometry and nomenclature. Boundary layer computational domain is 128×64 in the x and y directions, with 64×64 Fourier modes in x and y and 33 Chebyshev modes mapped in the normal (z) direction.

The Navier–Stokes equations are solved in rotational form,

$$\frac{dv}{dt} = v \times \omega - \nabla(\Pi) + 1/\mathrm{Re}\,\nabla^2(v)$$
$$\nabla \cdot (v) = 0 \tag{2.1}$$

where $\omega = \nabla \times v$ is the vorticity and $\Pi = P + v^2/2$. The velocities are normalized with respect to the centerline velocity in the channel and the free stream velocity in the boundary layer.

The spectral method of Orszag and Patera (1983) is used in both the channel and boundary layer calculations. For the boundary layer, the scheme is modified by mapping the Chebyshev collocation points of the channel to the desired locations in the boundary layer. A mapping function

$$z^* = f(z) \tag{2.2}$$

is chosen. When taking derivatives in the z direction (e.g., in calculating the vorticity) the Chebyshev differentiation in z^* is followed by the multiplication by $f'(z)$:

$$\frac{d}{dz} = \frac{df}{dz}\frac{d}{dz^*} \tag{2.3}$$

The boundary condition at infinity ($v_x = 1$) is implemented by recalculating the (0, 0) Fourier mode (the mean flow in x and y) in the viscous step. Symmetry is not imposed, but the spots develop symmetrically when symmetric initial conditions are used.

The disturbance is initiated by applying a body force to a packet of fluid for a short time interval, producing a small jet normal to and away from the wall. The form of the disturbance is Gaussian in x and y and continuous in time:

$$F = G(t)\, e^{[-r^2/2\sigma^2]} \tag{2.4}$$

where $G(t)$ is a ramp function and $r = (x^2 + y^2)^{1/2}$. The sizes of the jets are indicated in Table I.

Table I

	Channel	Boundary layer
σ	0.16	0.7
Location	$0.1 < z < 0.2$	$0.05 < z < 1.5$
Peak normal velocity	0.09	0.035

We impose the following boundary conditions on the flow through the channel: the velocity at the walls is zero, and the flow is periodic at the inflow–outflow and cross-stream boundaries. The flow is driven by a constant pressure gradient superimposed onto the periodic pressure component. The Reynolds number for the channel runs is 6000 based on the channel half-width. The Reynolds number for the boundary layer simulations is 1000 based on the boundary layer thickness corresponding to $\eta = 1.0$.

3. SPOTS IN CHANNEL FLOWS

In Fig. 7, we plot contours of the maximum (in y) of the absolute value of the normal velocity, $\mathrm{Max}_y|v_z|$ for a channel spot at $\mathrm{Re} = 6000$. The contour plots we present for channel spots encompass the entire $20 \times 5 \times 2$ computational domain; their dimensions are not to scale. Except where

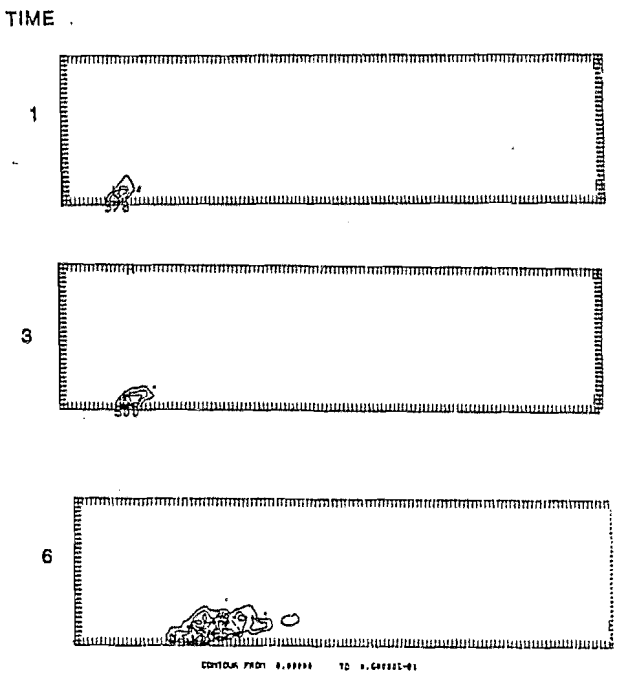

Fig. 7. Early-time evolution of channel spot. $\mathrm{Max}_y|v_z|$ contours are plotted at 1% intervals.

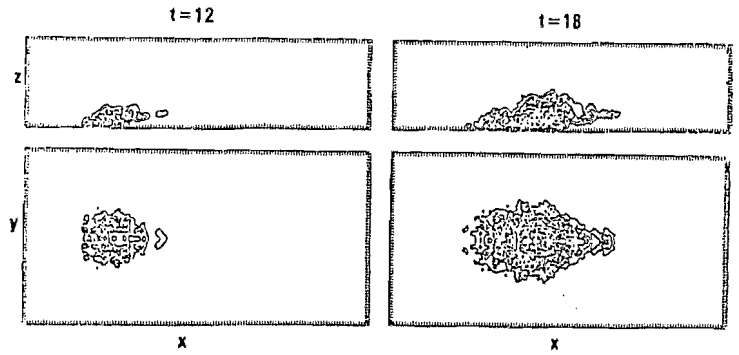

Fig. 8. Channel spot at intermediate times. $\mathrm{Max}_z|v_z|$ contours in (a) and (b); $\mathrm{Max}_y|v_z|$ contours in (c) and (d).

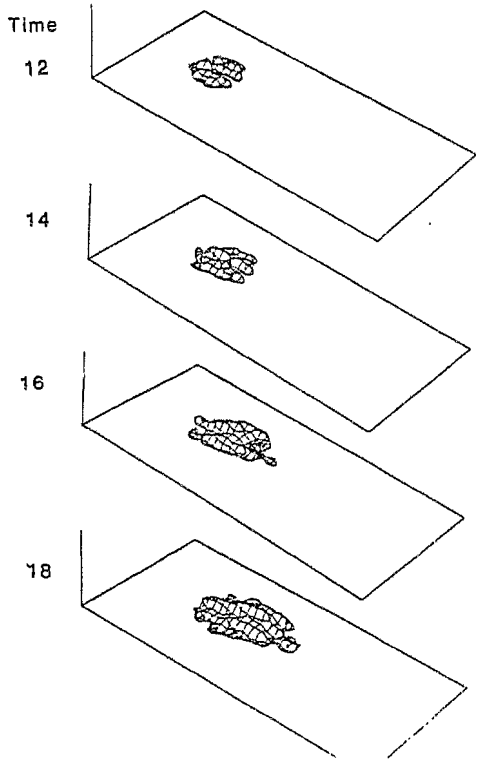

Fig. 9. Surfaces of 2% x-velocity perturbations in developing channel spot.

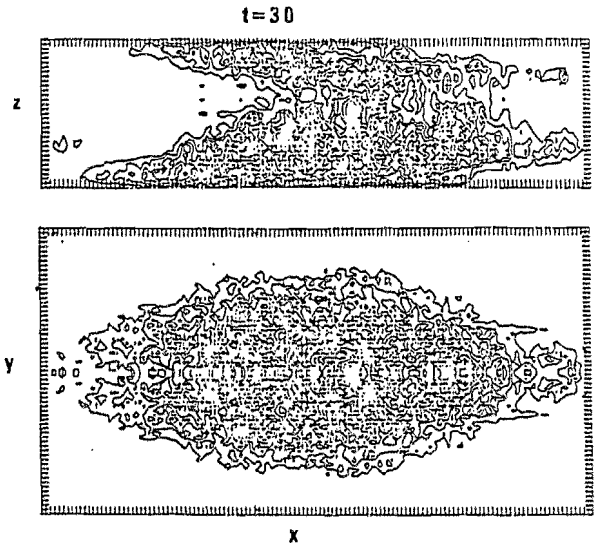

Fig. 10. Channel spot at $t = 30$. $\mathrm{Max}_z|v_z|$ contours in (a); $\mathrm{Max}_y|v_z|$ contours in (b).

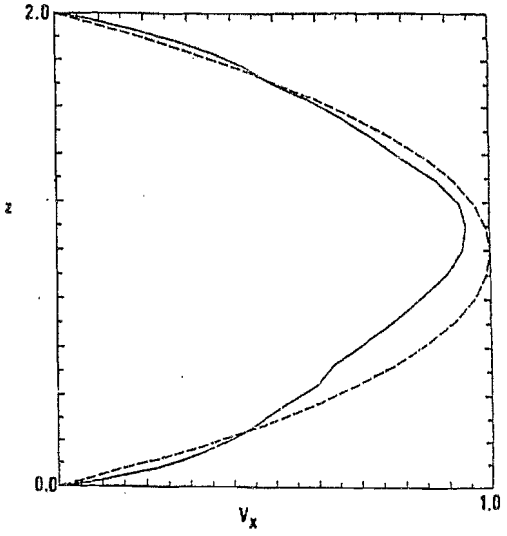

Fig. 11. Mean velocity profiles at center (solid) and edge (broken) of spot.

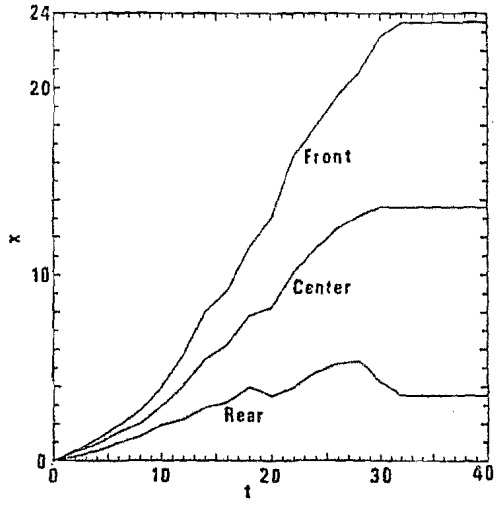

Fig. 12. Location in x of front, center, and rear of channel spot versus time, where spot is defined as region where $|v_z| \geq 2\%$. For t larger than 30, the spot length reaches the periodicity length of the computational domain, so the spot ceases to grow in the streamwise direction.

noted, the contours are at 1% intervals of $\mathrm{Max}_q|v_z|$, where q is the coordinate normal to the plotting plane. With this projection of the spot onto a plane we view the data from the experimentalist's perspective (with the line of sight extending all the way through the channel). At time $t=1$, the initial disturbance has convected downstream and has become slightly distorted. The initial peak velocity of 0.09 has decreased to 0.038 owing to the viscous diffusion. By a time of $t=3$, the velocity has increased to 0.05 due to instability in the flow. The disturbance is elongated in x as well as convected downstream. In Fig. 8 we see the disturbance develop most of the features characteristic of a spot. The front of the disturbance moves away from the wall. The disturbance grows in all directions and the "arrowhead"

Table II. Channel Spots

	Experimental	Computational
Velocity of Front	0.6	0.85
Rear	0.34	0.25
Spreading half-angle	8°	10°

shape becomes apparent. The peak normal velocity increases from 6% at $t=12$ to 9% at $t=18$.

In Fig. 9 we show the development of the boundaries with an isometric view. Enclosed within the surface is fluid whose x velocity differs from the Poiseuille profile by more than 2%.

The results plotted in Fig. 10 are $\mathrm{Max}_y|v_z|$ and $\mathrm{Max}_z|v_z|$. At $t=30$, the spot has fully extended through the channel with a peak normal velocity of 13%. The initial disturbance on the bottom wall has induced a new disturbance at the top wall. This second, smaller spot has a peak velocity that occurs at a distance of approximately 0.25 (1/8 channel width) away from the top wall. By $t=30$, the two spots have joined to produce a disturbance that fills the span of the channel.

In Fig. 11 we show the distortion of the Poiseuille profile at the spot center. The velocity at the edge is essentially unchanged from that of the

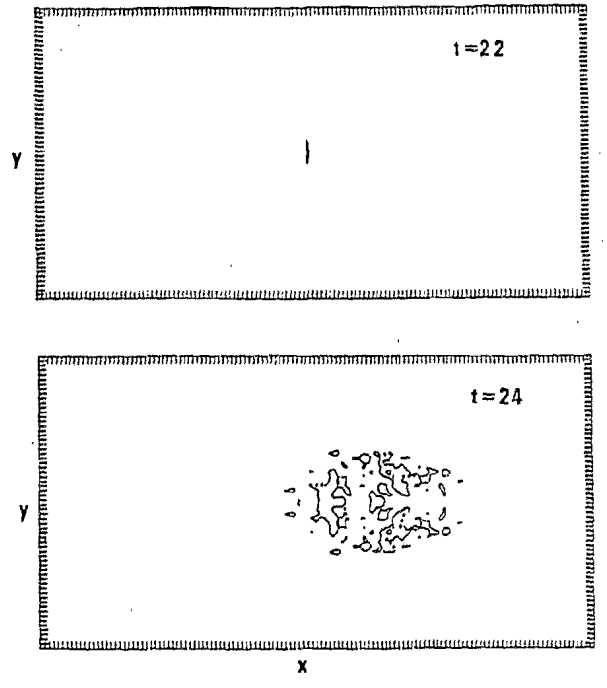

Fig. 13. Perturbation velocity, $v(x, t)$, contours at $t=22$ and $t=24$ for channel spot perturbed at its center at $t=20$.

original Poiseuille flow, while at the spot center there is a velocity defect of 0.1–0.2. At the bottom wall, the shear has increased by a factor of 3.

In Table II and Figure 12, we show how the spot geometry changes in time. Although there are significant differences between conditions generating our numerical spot and those generating the spots studied experimentally, a comparison of numerical and laboratory features is instructive. Carlson *et al.* (1982) generated spots in a laboratory channel flow at Re = 1000, while we used Re = 6000 in our calculations. Most of the experimental data were taken more than 50–100 channel widths downstream of the initial disturbance, while we have been able to follow the spot for only 10 channel widths. Further development of the channel spot would require a larger computational domain. The growth rate of the width and length of the numerical spot becomes constant at $t = 15$ and remains so until the spot fills the domain at $t = 32$. This steady growth rate

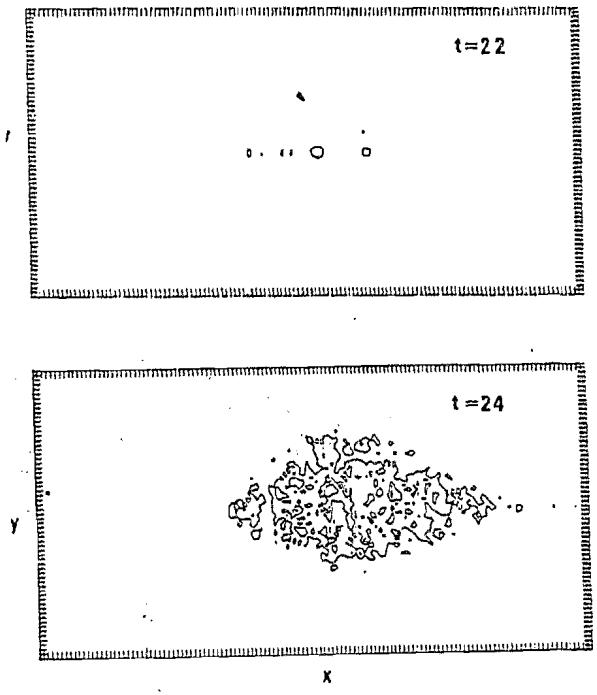

Fig. 14. Perturbation velocity, $\varepsilon(x, t)$, contours at $t = 22$ and $t = 24$ for channel spot perturbed at its edge at $t = 20$.

is slightly higher than that observed experimentally in both the lateral and longitudinal directions. This discrepancy can be due to the difference in Reynolds numbers or to the lack of maturity of our computed spots compared to those studied experimentally. We have not observed in our data any significant evidence of the leading Tollmien–Schlicting waves that were observed experimentally. Again, we believe that the absence of these waves is due to the lack of maturity of our computed spots.

A further numerical calculation is done to compare the stability characteristics of the spot at its edge and center. The velocity field of a spot at $t = 20$ is used as the initial condition for three runs. The first run consists of restarting the original spot calculation and allowing the spot to continue development undisturbed to a time of 24. For the second run, a disturbance is applied at $t = 20$ to the original spot at its center. This disturbance is of the same spatial and temporal extent as the original disturbance that initiated the spot, but the magnitude is 1/10 that of the original. The difference between the resulting velocity fields, $\varepsilon(x, t) = |v_{z1} - v_{z2}|$, is a measure of the effect of the disturbance. By $t = 24$, $\varepsilon(x, t)$ has exceeded 1% in the central 2/3 of the spot (Fig. 13). The third run is identical to the second, but with the disturbance applied at the spot edge, rather than at the center. At $t = 24$ the disturbance had propagated through most of the spot (see Fig. 14), and had a peak magnitude of about 4%, as opposed to the 1.5% peak from the second run.

From these results, we conclude that the channel spots are less stable at their edges than at their centers. This observation suggests that spots grow by destabilization of neighboring fluid, rather than simply engulfing laminar fluid.

4. SPOTS IN BOUNDARY LAYER FLOWS

In Figs. 15–17 we show the development of a boundary layer spot at Re = 1000 up to $t = 90$. The contour plots we present for boundary layer spots encompass the entire 128×64 computational domain in x and y and are truncated at $z = 22$. Again, except where noted, the contours are at 1%

Table III. Boundary Layer Spots

	Experimental	Computational
Velocity of Front	0.9	0.85
Rear	0.5	0.3
Spreading half-angle	10°	12°

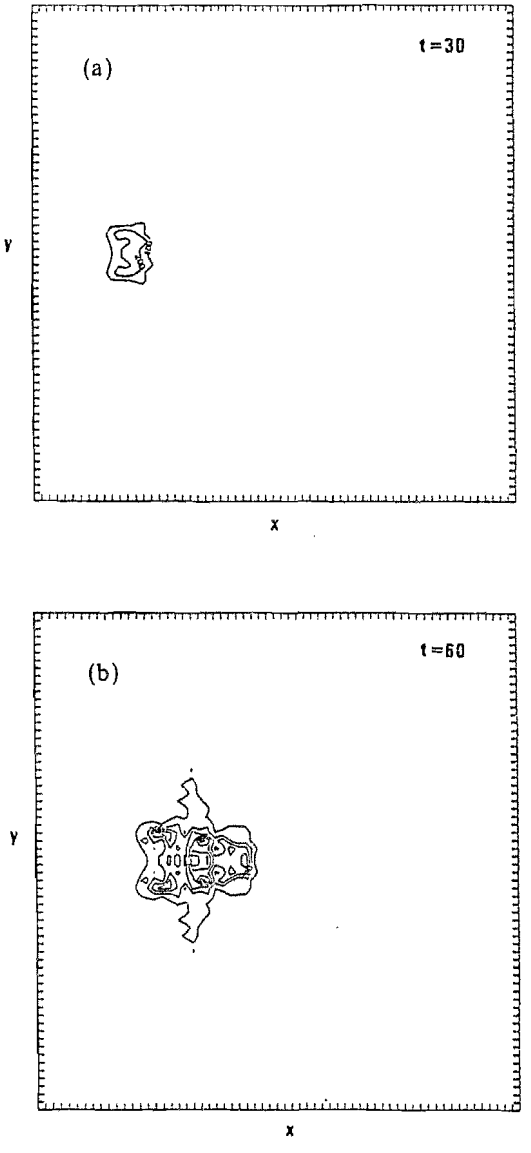

Fig. 15. Development of boundary layer spot. $\mathrm{Max}_z|v_z|$ contours are plotted at 1% intervals. (a) $t=30$; (b) $t=60$; (c) $t=90$.

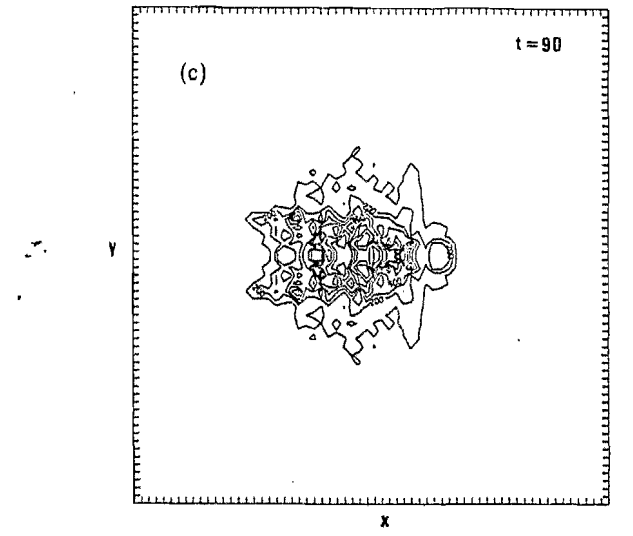

Fig. 15. Continued.

intervals of $\mathrm{Max}_q|v_z|$, where q is the direction normal to the plotting plane. The initial Blasius profile thickened with time. Figure 15 shows the streamwise and spanwise development of the spot from the initial disturbance. At $t=90$, the spot has begun to develop the characteristic arrowhead shape, which is more apparent in the second (2%) velocity contour. Figure 16 shows the overhang develop in the leading edge. Figure 17 shows the development of the triangular shape and the overhang in the spanwise direction.

The growth and development of the spot in a boundary layer is compared with the experimental findings of Wygnanski *et al.* in Table III. The growth rate of the spot in the streamwise and spanwise directions is in relatively close agreement with the experimental data. This suggests that the growth mechanisms in a boundary layer spot have been accurately captured in this simulation.

Figure 18 shows cross sections of the spot at $t=90$. Here we plot contours of the local values of v_z at $y-y_{\mathrm{center}}=0.5$, 2.5, and 4.5, in Figs. 18a, 18b, and 18c, respectively. Intervals are at 1% and dashed contour lines represent negative z velocities. The velocities are highest in the plane closest to the center of the spot (see Fig. 18a). Away from the spot center line the velocities and the spot height decrease. The front of the spot had an overhang of a distance of 10–20 in x, as has been observed experimentally.

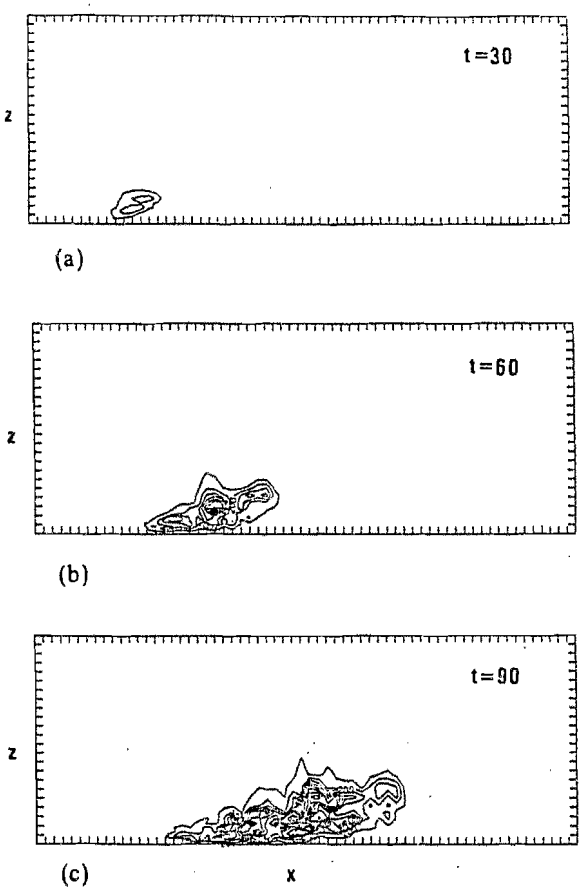

Fig. 16. Development of boundary layer spot. $\mathrm{Max}_x|v_z|$ contours are plotted at 1% intervals. (a) $t=30$; (b) $t=60$; (c) $t=90$.

The flow is dominated by eddies with length scales of approximately 10 in x and 5 in y. These length scales differ from those of unstable modes of the Orr–Sommerfeld equations, which predicts linear instability for much longer wavelengths, $30 < \lambda_x < 85$.

In order to explore the later time evolution of boundary layer spots, it will be necessary to use higher-resolution simulations, which we hope to perform in the future.

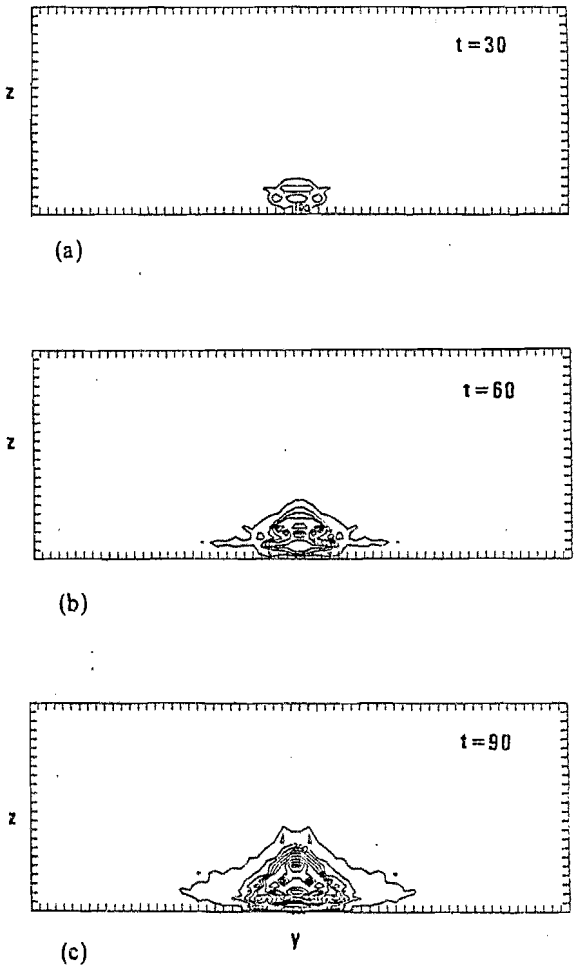

Fig. 17. Development of boundary layer spot. $\mathrm{Max}_x|v_z|$ contours are plotted at 1% intervals. (a) $t=30$; (b) $t=60$; (c) $t=90$.

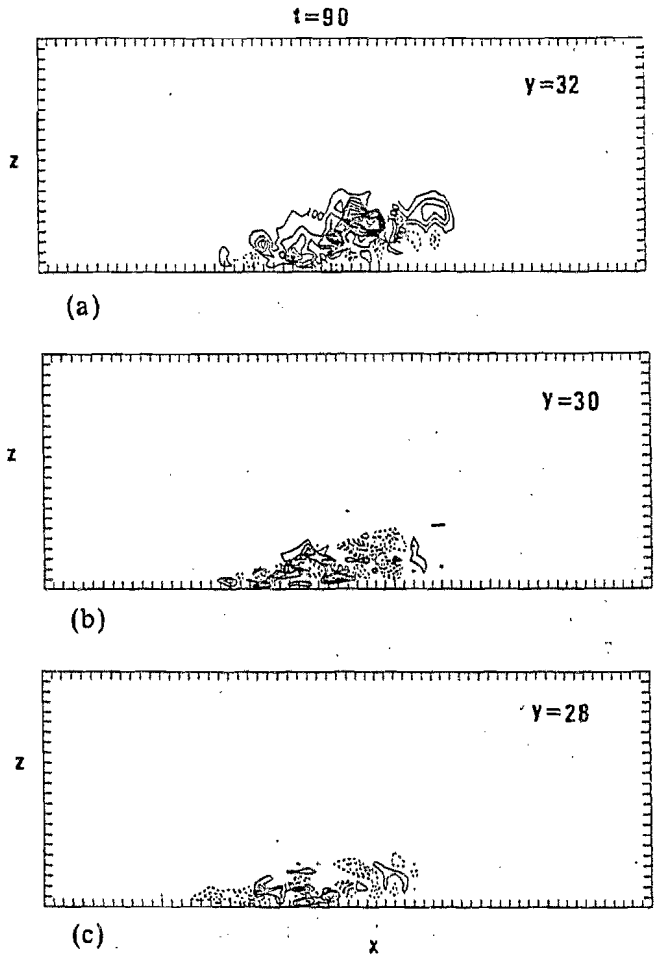

Fig. 18. Slices of spot at $t = 90$. Contours of v_z at $y = 32$, 30, and 28. The plane of symmetry of the spot is at $y = 32.5$. Dotted lines represent negative v_z.

5. CONCLUSIONS

It has been shown that spots can be generated by numerical solution of the Navier–Stokes equations. The fact that our results for the growth rates of the large-scale spot dimensions are relatively close to those seen experimentally suggests that the essential growth mechanisms of spots have been captured by our numerical experiments. These simulated spots are less mature than typical experimental spots, but their behavior appears to approximate that in a fully developed spot.

The spots generated were not dominated by two-dimensional Tollmein–Schlicting waves. This suggests that the growth in spots is not linear growth of two-dimensional Tollmein–Schlicting waves. Moreover, the perturbation velocities seen were about 0.1; perturbations this large would make the results of linear theory inapplicable and suggest domination of nonlinear effects. This does not rule out the importance of Tollmein–Schlicting waves in the amplification of small disturbances which may develop into spots or as a driving mechanism for some secondary instability in spots.

ACKNOWLEDGMENTS

The authors wish to thank Professor A. T. Patera for development of the original computer code modified for these calculations and for helpful discussions. This work was supported by the Air Force Office of Scientific Research under contracts Nos. F49620-83-C-0064 and F49620-85-C-0026 and the Office of Naval Research under contract No. N00014-82-C-0451.

REFERENCES

Balasubramanian, R., Orszag, S., Cary, A. M., Lin, J., and Walsh, M. (1988). to appear

Carlson, D. R., Widnall, S. E., and Peeters, M. F. (1982). A flow-visualization study of transition in plane Poiseuille flow, *J. Fluid Mech.* **121**, 487–505.

Elder, J. (1960). An experimental investigation of turbulent spots and breakdown to turbulence, *J. Fluid Mech.* **9**, 235–246.

Emmons, H. W. (1951). The laminar–turbulent transition in a boundary layer. Part I, *J. Aerosol. Sci.* **18**, 490.

Gad-el-Hak, M., Blackwelder, R., and Riley, J. J. (1981). On the growth of turbulent regions in laminar boundary layers, *J. Fluid Mech.* **110**, 73–96.

Gaster, M. (1975). A theoretical model of a wave packet in the boundary layer on a flat plate, *Proc. R. Soc. London* **347**, 271–289.

Gaster, M., and Grant, I. (1975). An experimental investigation of the formation and development of a wave packet in a laminar boundary layer, *Proc. R. Soc.* **347**, 253–269.

Leonard, A. (1981). Turbulent structures in wall-bounded shear flows observed via three-dimensional numerical simulations. In Jiminez, J. (ed.), *The Role of Coherent Structures in Modelling Turbulence and Mixing*. Lecture Notes in Physics, Vol. 136, Springer-Verlag, New York, pp. 119–145.

Orszag, S., and Patera, A. (1983). Secondary instability of wall-bounded shear flows, *J. Fluid Mech.* **128**, 347–385.

Wygnanski, I., Sokolov, M., and Friedman, D. (1976). On a turbulent spot in a laminar boundary layer. *J. Fluid Mech.* **78**, 785–819.